CrystEngComm

ROYAL SOCIETY OF CHEMISTRY

PAPER

View Article Online
View Journal | View Issue

Cite this: *CrystEngComm*, 2024, **26**, 4833

Equilibrium and non-equilibrium lattice structure, ferrimagnetic spin order and electrical conductivity at high-temperature regime of single-phased and bi-phased Co-rich spinel ferrites

Rabindra Nath Bhowmik, *[a] Vimal Narayan Sahoo,[a] Peram Delli Babu, [b] Anil K. Sinha[cd] and Abhay Bhisikar[c]

Received 20th March 2024,
Accepted 6th August 2024

DOI: 10.1039/d4ce00278d

rsc.li/crystengcomm

This work investigates the role of stable (sing-phased) and unstable (bi-phased) lattice structures in controlling the magnetic spin order and electronic properties in Co-rich ferrites of compositions $Co_{1.25}Fe_{1.75}O_4$ and $Co_{2.25}Fe_{0.75}O_4$. The material was synthesized *via* the chemical reaction of metal (Co and Fe) nitrates in an alkaline medium and post-heat treatment. The XRD patterns of $Co_{1.25}Fe_{1.75}O_4$ showed a single-phased structure upon heat treatment in the temperature range of 200–900 °C, whereas $Co_{2.25}Fe_{0.75}O_4$ showed a single-phased structure at 900 °C and bi-phased structure at a low heating temperature range of 200–800 °C. The thermally induced irreversibility (non-equilibrium) effect was observed in the lattice structure, magnetic spin order and electrical conductivity. The lattice structure at the (local) microscopic scale showed a more or less metastable state and coexistence of mixed-charge states of Co and Fe ions, irrespective of the single or bi-phased structure. The magnetic and electronic responses are found to be sensitive enough to detect local level non-equilibrium (metastable) states in non-equilibrium and equilibrium crystalline phases seen from XRD patterns.

1. Introduction

Electronic spin order and charge conductivity are strongly correlated in the equilibrium and non-equilibrium lattice structure of Co-rich spinel ferrites ($Co_xFe_{3-x}O_4$; $1 < x < 3$).[1–3] A stable equilibrium state of lattice structures exists when a system attains its lowest chemical (Gibbs) potential energy and a non-equilibrium state forms when the system is energetic at the saddle point of the potential energy curve and perturbed from its true (stable) equilibrium state.[4] If the perturbation is too small, the equilibrium state can be re-established by the removal of excess energy, and the process can be approximated as reversible. The system can attain an unstable state when the extra energy reaches beyond a certain limit of non-equilibrium conditions or reaches the top of the chemical potential energy curve during structural phase formation. In such a case, the thermodynamic process follows an irreversible path during the removal of the perturbed energy. The chemical potential energy of the system is lowered from the unstable state through the spontaneous decomposition (split) of the lattice structure to two phases with variations in local chemical composition. Such structural phase split without nucleation is known as spinodal decomposition in Co-rich spinel ferrites.[5–8] The Co content and heat treatment temperature during material preparation act as major thermodynamic forces to determine equilibrium and non-equilibrium lattice structures. The Co-rich spinel ferrites, whose composition lies in the miscibility gap of the Fe_3O_4–Co_3O_4 system, are kinetically sensitive to heat treatment temperatures in the range of 900–950 °C to form a stable and single-phased lattice structure. Beyond this critical temperature range, the Co-rich ferrites showed spinodal decomposition into Co- and Fe-rich cubic spinel phases.[9] The distribution of Co and Fe ions at the A (tetrahedral) and B (octahedral) sites in a bi-phased cubic spinel structure differs from that in a stable and single-phased lattice structure. The Co-rich phase (phase 1) has been defined as the cubic spinel phase that contains more number of total Co ions in the formula unit, and the Fe-rich phase (phase 2) has been defined as the cubic spinel phase that contains more number of Fe ions in the formula unit with reference to the total

[a] *Department of Physics, Pondicherry University, R.V. Nagar, Kalapet, Pondicherry 605014, India. E-mail: rnbhowmik.phy@pondiuni.edu.in; Tel: +91 9944064547*
[b] *UGC-DAE Consortium for Scientific Research, Mumbai Centre, Bhabha Atomic Research Centre, Trombay, Mumbai-400085, India*
[c] *HXAL, SUS, Raja Ramanna Centre for Advanced Technology, Indore-452013, India*
[d] *Department of Physics, School of Engineering, University of Petroleum and Energy studies, Dehradun-248007, Uttarakhand, India*

number of Co and Fe ions in a single-phased sample prepared *via* heat treatment at 900 °C.[10–12] The study of spinodal decomposition in Co-rich spinel oxides is interesting for tuning the properties of the intrinsic non-equilibrium structure, where phase fractions are sensitive to externally applied magnetic fields, and such materials are useful for developing high entropy energy storage devices.[8,13–15] However, the response of metastable phases during the time and high-temperature variation of the measurement has not been well investigated.

O'Neill *et al.*[16] showed a thermal cycle-induced cation order–disorder effect in Mg_2TiO_4. The distribution of Mg^{2+} and Ti^{4+} ions formed an ordered state of inverse structure (all Ti^{4+} ions occupying half of the B sites) during the warming mode from 300 K to 1173 K and a disordered state (migration of a fraction of Ti^{4+} to A sites) at higher temperatures. The reordering of cations at the A and B sites during the cooling mode was faster, and the high-temperature disordered state was not preserved after cooling back to 300 K. The thermal cycling-induced lattice disorder perturbed the equilibrium state of the cation order at A- and B-sites in the spinel structure.[17–19] The irreversibility in magnetic exchange interactions and spin order exhibited unusual magnetic properties (magnetic blocking, exchange bias) at low temperatures, which are different from high-temperature magnetic phases.[20,21] The study of the relationship between non-equilibrium lattice structure and physical (electrical and magnetic) properties from high-temperature measurements is limited in the literature[10,22] but useful for high-temperature applications of the material in magneto-electric memory devices.[8,23–25]

We investigate the effects of equilibrium and non-equilibrium lattice structures in Co-rich spinel ferrite of compositions $Co_{1.25}Fe_{1.75}O_4$ and $Co_{2.25}Fe_{0.75}O_4$ on the high-temperature magnetic and semiconductor properties. We highlight the role of the measurement temperature cycle-induced metastable state in the lattice structure in producing the irreversibility in magnetic and electrical conductivity curves. The irreversibility means a noticeable difference in the values of physical parameters (lattice parameter, magnetization, electrical conductivity) during the warming and cooling modes of the measurement temperature variation. The results can be used as an alternative technique to distinctly differentiate the effect of the non-equilibrium (metastable) phase observable from the X-ray diffraction pattern and the local level (transient) metastable state not observable from the X-ray diffraction pattern of the single- or bi-phased lattice structure of materials.

2. Experimental

A. Sample preparation

The $Co_{1.25}Fe_{1.75}O_4$ and $Co_{2.25}Fe_{0.75}O_4$ compositions were synthesized by following the chemical co-precipitation route, where a better chemical homogeneity is expected at the atomic level of the compound. The required amounts of $Co(NO_3)_2{\cdot}6H_2O$ and $Fe(No_3)_3{\cdot}9H_2O$ nitrate salts were dissolved in distilled water. The NaOH solution with an initial pH of ~13 was added gradually into the nitrate solution to maintain the final pH value at ~11 during the chemical reaction. The reaction temperature was maintained at 80 °C with continuous magnetic stirring. The products were allowed to cool down to room temperature and allowed to precipitate at the bottom of a Borosil beaker. The transparent solution was removed carefully from the top of the precipitate, and the remaining product was washed several times with distilled water. At each time, the product was dried at 100 °C. The resultant powder was heated at 200 °C to confirm a complete removal of the bi-product of $NaNO_3$, which formed a white coating on the wall of the beaker, and black coloured (magnetic) powder was collected at the center of the beaker when placed on a Rotamantle. The black powder was made into several pellets and heated in the range of 200–900 °C for 6 h. The samples were denoted as C125F175_20, C125F175_50, C125F175_80 and C125F175_90 for the heat treatment temperature at 200 °C, 500 °C, 800 °C and 900 °C, respectively, for the $Co_{1.25}Fe_{1.75}O_4$. The $Co_{2.25}Fe_{0.75}O_4$ samples were denoted as C225F75_20 and C225F75_90 for heat treatment temperatures at 200 °C and 900 °C, respectively. The heating and cooling rate of the samples in the air during heat treatment was maintained@5 °C min^{-1}.

B. Sample characterization

The synchrotron X-ray diffraction (SXRD) patterns were recorded in the 2θ range 5–40° using synchrotron radiation (λ ~ 0.8360 Å) at the angle dispersive X-ray diffraction beamline (BL-12) in Indus-2, Indore, India. The sample-to-detector distance for SXRD was calibrated by using a standard Si powder sample. The SXRD patterns were recorded in the warming mode of high-temperature variation from 300 K to 873 K and cooling back to 373 K@20 K min^{-1} in air. The sample was waited for 5 min. to stabilize the temperature before the measurement of data at each temperature for 2–3 min. The survey scans of X-ray photoelectron spectra (XPS) were recorded in the range of 0–1350 eV with step size 1.0 eV, and narrow scans for specific XPS bands of the ions were recorded with a step size 0.1 eV by using a thermos-scientific instrument (model: K-Alpha-KAN9954133) with a monochromatic Al-K_α source. The temperature-dependent magnetization [$M(T)$] in the magnetic field warming (MFW: 300–950 K) and cooling (FCW: 950–300 K) modes were measured using a physical property measurement system (PPMS-EC2, Quantum Design, USA). The temperature varied@5 K min^{-1} with a waiting time of 2 min before recording the $M(T)$ data in the presence of a 500 Oe field at each temperature. After MFW(T) measurement in the presence of a 500 Oe field at 300 K, the magnetic field-dependent magnetization [$M(H)$] curves were recorded within the field range of ±70 kOe at selected temperatures in the range of 300 K to 900 K during the warming mode. The

current–voltage (I–V) characteristics were measured in the temperature range of 300–623 K using a Keithley 6517B high resistance meter. The disc-shaped samples (∅ = 10 mm, t ∼ 0.5 mm) were placed between two Pt electrodes of a homemade sample holder to make a Pt/sample/Pt device structure. The I–V curves were measured by sweeping the bias voltage within ±50 V depending on the sample and measurement temperature. The temperature varied@5 K min^{-1} with a waiting time of 2–3 min before recording the I–V curve at each temperature for a time ≤2 min. The measurement protocols were maintained uniformly for all the pellet-shaped samples. The total time at each temperature (<10 min including waiting time) during the measurement of SXRD and physical properties was much less than the heat treatment time (6 h) during the structural phase formation of the material.

3. Results

A. Synchrotron X-ray diffraction

SXRD patterns of the samples (in Fig. 1 and 2) at the selected temperatures (300–873 K) during warming and cooling modes are consistent with a cubic spinel structure (space group $Fd\bar{3}m$).[11,12] Rietveld refinement of the SXRD patterns was performed by using a mixed cubic spinel structure model

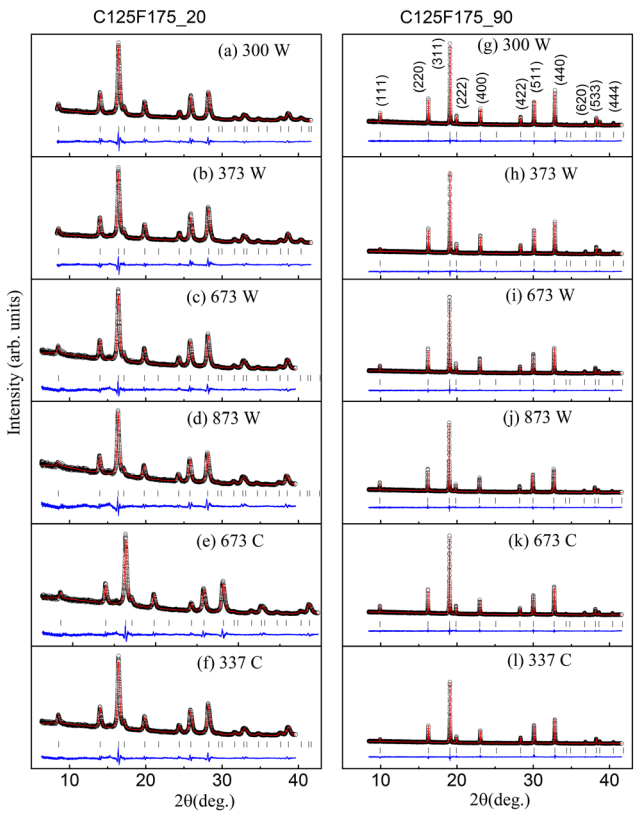

Fig. 1 Refined SXRD patterns for samples C125F175_20 (a–f) and C125F175_90 (g–l) measured in the warming (W) and cooling (C) modes of temperature variation. Miller indices for the cubic spinel structure are indicated in (g).

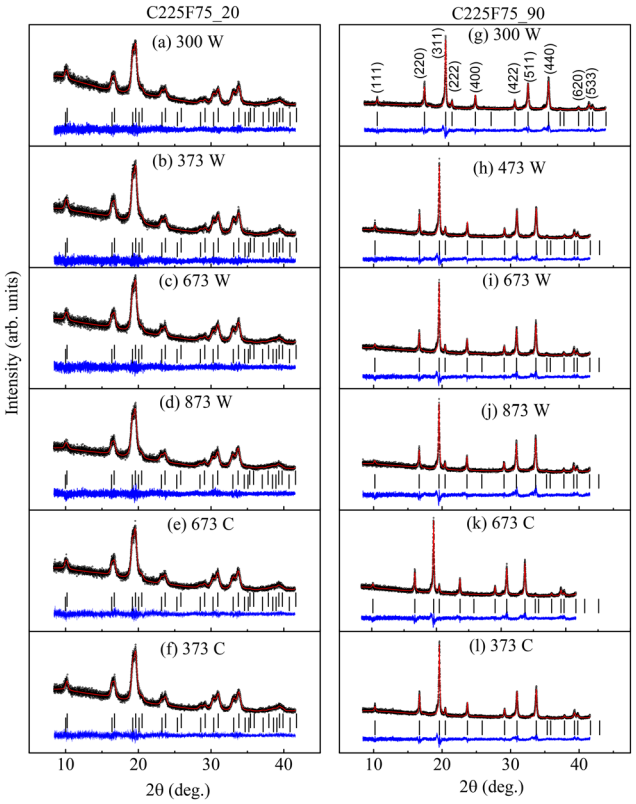

Fig. 2 Refined SXRD patterns of samples C225F75_20 (a–f) and C225F75_90 (g–l) during warming (W) and cooling (C) modes of temperature variation. Miller indices for cubic spinel structure are indicated in (g).

$(Co^{2+}_{1-\beta}Fe^{3+}_{\beta})_A[Co^{2+}_{\beta}Co^{3+}_{x-1}Fe^{3+}_{3-x-\beta}]_BO_4$ for $Fe_{3-x}Co_xO_4$ ferrite ($0 \le \beta \le 1$; $1 < x < 3$) with space group $Fd\bar{3}m$. The Wyckoff positions at the A (8a) sites (1/8, 1/8, 1/8) were co-occupied by Co^{2+} and Fe^{3+} ions and the B (16d) sites (1/2, 1/2, 1/2) were co-occupied by Co^{2+}/Co^{3+} and Fe^{3+}/Fe^{2+} ions, and the 32e sites were occupied by oxygen (O^{2-}) ions. The structural parameters such as lattice parameter (a), cell volume (V), oxygen parameter (u), site distribution of Co and Fe ions, oxygen stoichiometry and the shape parameters were suitably varied to obtain the best fit. The initial values of structural parameters for the refinement were matched to the values for some of the samples from previous works using refinement of SXRD patterns and neutron diffraction patterns at 300 K.[11,12,26,27] Then, refinement of the SXRD pattern at higher temperatures was carried out by considering the single-phased and bi-phased (Co- and Fe-rich cubic spinel phases) structure. SXRD patterns of the (C125F175_20 and C125F175_90) $Co_{1.25}Fe_{1.75}O_4$ samples were fitted with a single-phased structure. SXRD patterns of the $Co_{2.25}Fe_{0.75}O_4$ samples were fitted with Co- and Fe-rich cubic spinel phases for heat treatment at 200 °C (C225F75_20 sample) and single-phased structure for heat treatment at 900 °C (C225F75_20 sample). The values of structural parameters and site distribution of cations are well-matched to the previous works.[11,27] The refinement results at a measurement

Table 1 Structural parameters from Rietveld refinement parameters of SXRD data at 873 K

(a) Single-phase model of the cubic spinel structure of C125F175_20 and C125F175_90 samples

Atoms (sites)	C125F175_20 Wyckoff positions X	Y	Z	B	Occupancy	C125F175_90 Wyckoff positions X	Y	Z	B	Occupancy
Co (8a)	0.12500	0.12500	0.12500	0.997	0.520(38)	0.12500	0.12500	0.12500	0.997	0.345(45)
Fe (8a)	0.12500	0.12500	0.12500	0.997	0.480(38)	0.12500	0.12500	0.12500	0.997	0.655(45)
Fe (16d)	0.50000	0.50000	0.50000	0.980	1.270(38)	0.50000	0.50000	0.50000	0.980	1.095(45)
Co (16d)	0.50000	0.50000	0.50000	0.980	0.730(38)	0.50000	0.50000	0.50000	0.980	0.905(45)
O (32e)	0.25452(24)	0.25452(24)	0.25452(24)	0.781	3.974(18)	0.25496(30)	0.25496(30)	0.25496(30)	0.781	3.943(22)
Cell parameters: a = 8.36245(45) Å, V = 584.791(55) Å^3						Cell parameters: a = 8.33860(12) Å, V = 579.802(15) Å^3				
R_p: 4.41 R_{wp}: 5.58 R_{exp}: 2.56 χ^2: 4.77						R_p: 8.18 R_{wp}: 10.40 R_{exp}: 7.76 χ^2: 1.80				

(b) Two-phase model of the cubic spinel structure of the C225F75_20 sample

Atoms (sites)	Co rich Wyckoff positions X	Y	Z	B	Occupancy	Fe rich Wyckoff positions X	Y	Z	B	Occupancy
Co (8a)	0.12500	0.12500	0.12500	0.997	0.484(91)	0.12500	0.12500	0.12500	0.997	0.464(82)
Fe (8a)	0.12500	0.12500	0.12500	0.997	0.552(91)	0.12500	0.12500	0.12500	0.997	0.555(82)
Fe (16d)	0.50000	0.50000	0.50000	0.980	0.148(91)	0.50000	0.50000	0.50000	0.980	0.245(82)
Co (16d)	0.50000	0.50000	0.50000	0.980	1.816(91)	0.50000	0.50000	0.50000	0.980	1.736(82)
O (32e)	0.25632(57)	0.25632(57)	0.25632(57)	0.786	3.974(18)	0.25441(26)	0.25441(26)	0.25441(26)	0.781	3.967(25)
Cell parameters: a = 8.10382(27) Å, V = 532.19(4) Å^3						Cell parameters: a = 8.27657(15) Å, V = 566.95(8) Å^3				
R_p: 6.66 R_{wp}: 8.60 R_{exp}: 8.52 χ^2: 1.02										
Co rich phase (Bragg factor 3.00, phase fraction 54.83(0.86)%)										
Fe rich phase (Bragg factor 3.97, phase fraction 45.17(0.87)%)										

(c) Variation in phase fraction with temperature of C225F75_20 and single-phase model of the cubic spinel structure of the C225F75_90 sample

T (K)	C225F75_20 (phase fraction %) Co rich Warming	Co rich Cooling	Fe rich Warming	Fe rich Cooling
300	54.32(1.02)	54.32	45.68(0.92)	45.68
373	53.36(1.02)	53.98(0.81)	46.64(1.01)	46.02(0.86)
473	55.25(0.83)	54.91(0.84)	44.75(0.83)	45.09(0.82)
573	53.29(0.84)	55.66(0.8)	46.71(0.87)	44.34(0.8)
673	54.85(0.83)	54.6(1.05)	45.15(0.84)	45.4(1.04)
773	55.84(0.82)	56.29(1.11)	44.16(0.82)	43.71(1.1)
873	54.83(0.86)	54.83(0.86)	45.17(0.87)	45.17(0.87)

C225F75_90

Atoms (sites)	Wyckoff positions X	Y	Z	B	Occupancy
Co (8a)	0.12500	0.12500	0.12500	0.997	0.731(79)
Fe (8a)	0.12500	0.12500	0.12500	0.997	0.298(79)
Fe (16d)	0.50000	0.50000	0.50000	0.980	0.452(79)
Co (16d)	0.50000	0.50000	0.50000	0.980	1.519(79)
O (32e)	0.25755(52)	0.25755(52)	0.25755(52)	0.781	4.014(24)
Cell parameters: a = 8.21512(55) Å, V = 554.424(64) Å^3					
R_p: 11.2 R_{wp}: 14.2 R_{exp}: 10.45 χ^2: 1.84					

temperature of 873 K have been summarized in Table 1. The samples confirmed a mixed-spinel structure, where Co and Fe ions occupied both A and B sites, irrespective of the single- or bi-phased structure. The site occupancy of Co and Fe ions varied depending on the chemical composition, heat treatment temperature and single or two-phased structures of the samples. For example, the Fe/Co ratio at the A sites increased by increasing the heat treatment temperature of the sample from 200 °C to 900 °C for $Co_{1.25}Fe_{1.75}O_4$. In the bi-phased structure of the C225F75_20 sample, the Co-rich phase (phase 1) contained more Co ions, and the Fe-rich phase (phase 2) contained more Fe ions in the cubic spinel structure unit with reference to the site-distributions in the stable single-phased C225F75_90 sample (where population of the A sites mostly dominated by the Co ions and Fe ion population at the B sites is relatively more than A sites). The A-site population of the Co ions in the single-phased C225F75_20 sample is also higher in comparison to the single-phased C125F175_20 sample and *vice versa* for the B-site population of Fe ions. The oxygen (O) content of the samples at 300 K per formula unit of the cubic spinel structure nearly matched the ideal value, whereas a slight variation in the O content was noted at 873 K.

Fig. 3 shows the variation of cell volume V and oxygen parameter (u) during warming and cooling modes of measurement temperatures. The samples showed nearly a linear thermal expansion of cell volume. The cell volume followed nearly reversible paths within the error bar in the single-phased C125F175_90 and C225F75_90 samples, whereas cooling and warming paths have noticeably differed well beyond the error bar in the intermediate temperature range (473–773 K) for the (single-phased C125F175_20 and bi-phased C225F75-20) samples prepared at low temperature (200 °C) heat treatment. However, none of the present samples show any intermediate structural destabilization by forming a CoO-like phase, as seen for $Co_{2.75}Fe_{0.25}O_4$ having

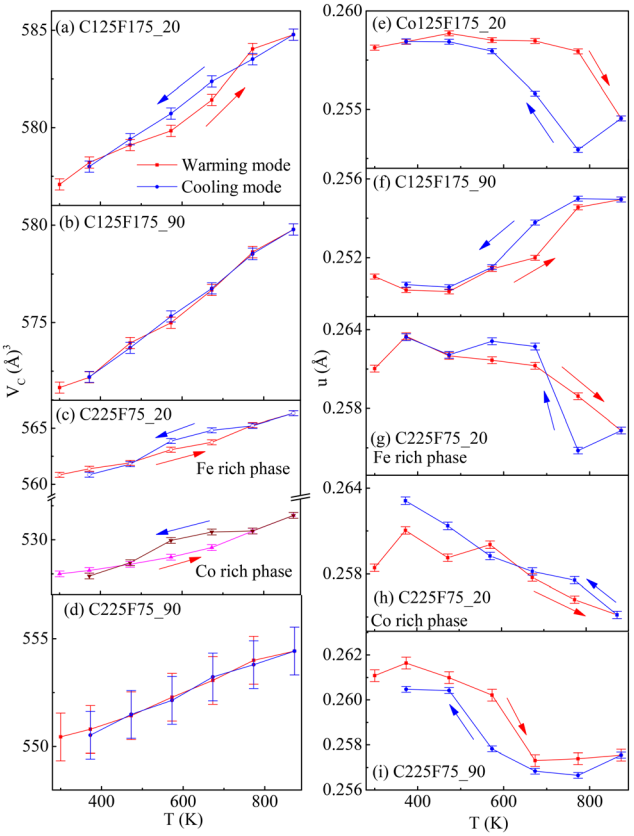

Fig. 3 The variation in the cell volume (a–d) and oxygen parameter (e–i) with temperature for the C125F175 and C225F75 samples.

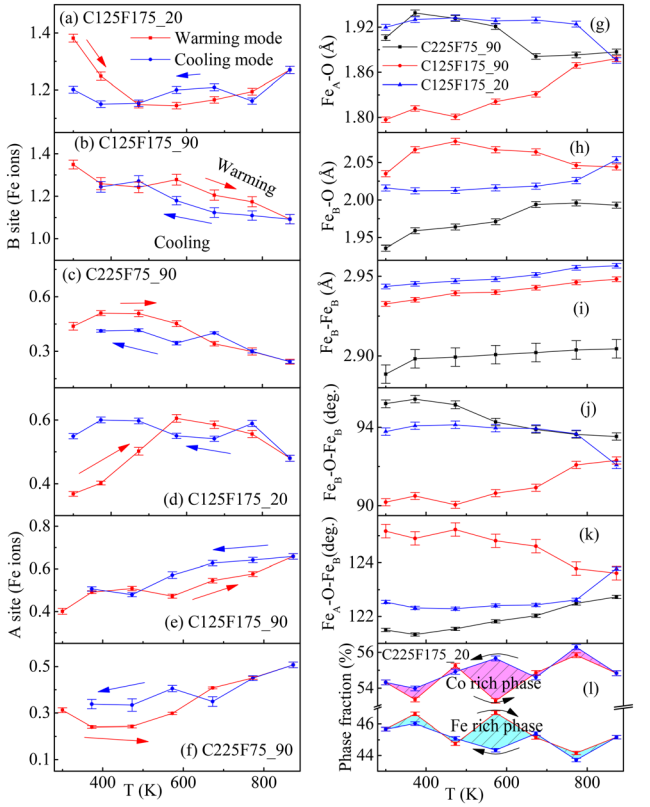

Fig. 4 B site (Fe ions) distribution (a–c), A site (Fe ions) distribution (d–f), different bond lengths and angles of all compositions (g–k) and the phase fractions in bi phased composition (l) with temperature variation.

an extremely high Co/Fe ratio.[21] The oxygen parameter (u), a microscopic displacement of the O ions with reference to a regular tetrahedron at the 8a sites and an octahedron at the 16d sites in the cubic spinel structure, varied in the range (0.252–0.264) of spinel oxides.[28,29] In the present spinel oxides, the oxygen parameter (u) during warming and cooling modes followed irreversible paths irrespective of single or bi-phased samples. The $u(T)$ values in $Co_{2.25}Fe_{0.75}O_4$ have decreased on increasing the temperature, whereas the u values in $Co_{1.25}Fe_{1.75}O_4$ showed a decrement at higher temperatures for the C125F175_20 sample and an increment for the C125F175_90 sample. The variation in u and lattice parameter (a) values can affect the M–O (metal–oxygen) bond lengths at the A sites $\left(R_{\text{tet}} = a\sqrt{3}\left(u - \frac{1}{8}\right)\right)$ and B sites $\left(R_{\text{oct}} = a\sqrt{\left(3u^2 - 2u + \frac{3}{8}\right)}\right)$.[28] In the mixed spinel structure, the radius of oxygen ion is assumed to be R_0 = 1.38 Å and the radii of Co ions (~0.545 Å for B site low-spin Co^{3+}, ~0.61 Å for B site high-spin Co^{3+}, ~0.745 Å for B site high-spin Co^{2+}, and ~0.58 Å for A site high-spin Co^{2+}) and Fe ions (~0.645 Å for B site high-spin Fe^{3+}, ~0.55 Å for B site low-spin Fe^{3+}, and ~0.49 Å for A site high-spin Fe^{3+}) varied depending on the charge state, magnetic spin state and site-occupancy. An increase in low spin Co^{3+} ions at the B sites reduces the lattice parameter (in $Co_{2.25}Fe_{0.75}O_4$ composition) and an increase in high spin Fe^{3+} ion occupancy at the B sites increases the lattice parameter (in $Co_{1.25}Fe_{1.75}O_4$ composition) in Co-rich ferrites.[5,6,8] The samples showed a non-negligible variation in the occupancy and thermally induced irreversibility in the site-occupancy of the Fe (B-sites) and Fe (A-sites) ions (in Fig. 4(a–f)) during warming and cooling paths of the temperature variation. Subsequently, the Fe–O bond lengths and Fe–O–Fe bond angles showed a noticeable change during temperature variation in the warming mode (Fig. 4(g–l)). The strength of inter and intra-sublattice (A–O–B, B–O–B and A–O–A) magnetic superexchange interactions is directly proportional to the bond angle and inversely proportional to the bond length between cations and oxygen ions.[30] The Fe–O bond lengths were found in the range of 1.80–1.940 Å and 1.92–2.060 Å for the A and B sites, respectively, whereas the Fe–Fe bond lengths at the B-sites were found in the range of 2.88–2.90 Å. The Fe_A–O bond length in the C125F175_20 sample is nearly temperature-independent (~1.930 Å) up to 773 K. It reduces to ~1.880 Å at 873 K. In the C125F175_90 sample, the Fe_A–O bond length increased from 1.80 Å at 300 K to 1.88 Å at 873 K. The Fe_A–O bond length in the C225F75_90 sample slowly decreased from 1.94 Å at lower temperatures to ~1.88 Å in

the temperature range of 673–873 K. The reverse trend was found for the Fe_B–O bond length, where it shows a thermal expansion for the C125F175_20 and C225F75_90 samples and a compression at higher temperatures for the C125F175_90 sample. The Fe_B–Fe_B bond length showed thermal expansion for all samples. The bond angles (<Fe_A–O–Fe_B and (<Fe_B–O–Fe_B) noticeably varied with temperature. The <Fe_B–O–Fe_B varied within 90–95° and <Fe_B–O–Fe_A varied within 121–125°. These angles lie in a typical range where superexchange interactions between A- and B-sites or intra-sub lattices (B–B) are diluted in a ferrimagnetic structure of cubic spinel oxide, whereas a long-ranged collinear ferrimagnetic structure assumes <Fe_B–O–Fe_B ~90° and <Fe_B–O–Fe_A ~125–180°. In the C125F175-20 sample, both <Fe_B–O–Fe_B and <Fe_B–O–Fe_A varied a little up to 773 K. At 873 K, <Fe_B–O–Fe_B noticeably decreased by increasing the <Fe_B–O–Fe_A angle. A gradual increase in the <Fe_B–O–Fe_B angle with temperature is accompanied by a decrease in the <Fe_B–O–Fe_A angle for the C125F175_90 sample. The <Fe_B–O–Fe_B and <Fe_B–O–Fe_A bond angles showed opposite temperature-dependent behavior in the C225F75_90 sample. In the bi-phased C225F75_20 sample (Fig. 4(l)), the fraction of the Co-rich phase increased from 54% to 56% by decreasing the Fe-rich phase fraction from 46% to 44% during the increase in the measurement temperature from 300 K to 875 K. The bond length, bond angles, phase fractions and charge state of metal ions are the factors that primarily control the magnetic and electrical properties, which are discussed below.

B. X-ray photoelectron spectra

X-ray photoelectron spectra (XPS) were recorded to study the surface chemical state (chemical structure and charge state of Co and Fe ions) of the samples. The spectra were recorded before etching and after etching of the surface under Ar sputtering for 60 s. We discuss the results from spectra recorded after etching. The atomic ratio of Co and Fe was determined from the survey scans of Co 2p and Fe 2p spectra. The measurements were repeated at least two times and cross-checked from the area of peak components in the narrow scanned Co 2p and Fe 2p spectra. The average Co : Fe ratio was found to be 1.21 : 1.79, 1.30 : 1.70, 2.13 : 0.87 and 2.18 : 0.82 for the samples C125F175_20, C125F175_90, C225F75_20 and C225F75_90, respectively. The difference in the atomic ratio from XPS from the exact stoichiometric ratio of the compounds can be associated with the accuracy of the fitted curve area. The oxygen content cannot be determined accurately from XPS due to additional contributions apart from the bonded oxygen to metal ions in the lattice structure. The line scans of the elemental Co 2p, Fe 2p and O1s spectra at 8 different points over a length of 600 μm were recorded to understand the surface nature of the samples. The primary peak component in the line scans of O 1s spectra (Fig. 5(a–d)) at binding energy (B. E.) of ~530.50–531.70 eV appears due to lattice oxygens in the M–O bonds of the cubic spinel lattice structure and a secondary peak component/hump at B.E. ~532–533 eV suggests surface defects (oxygen vacancy or adsorbed hydroxyl groups) in the samples.[31–34] The surface defects/non-

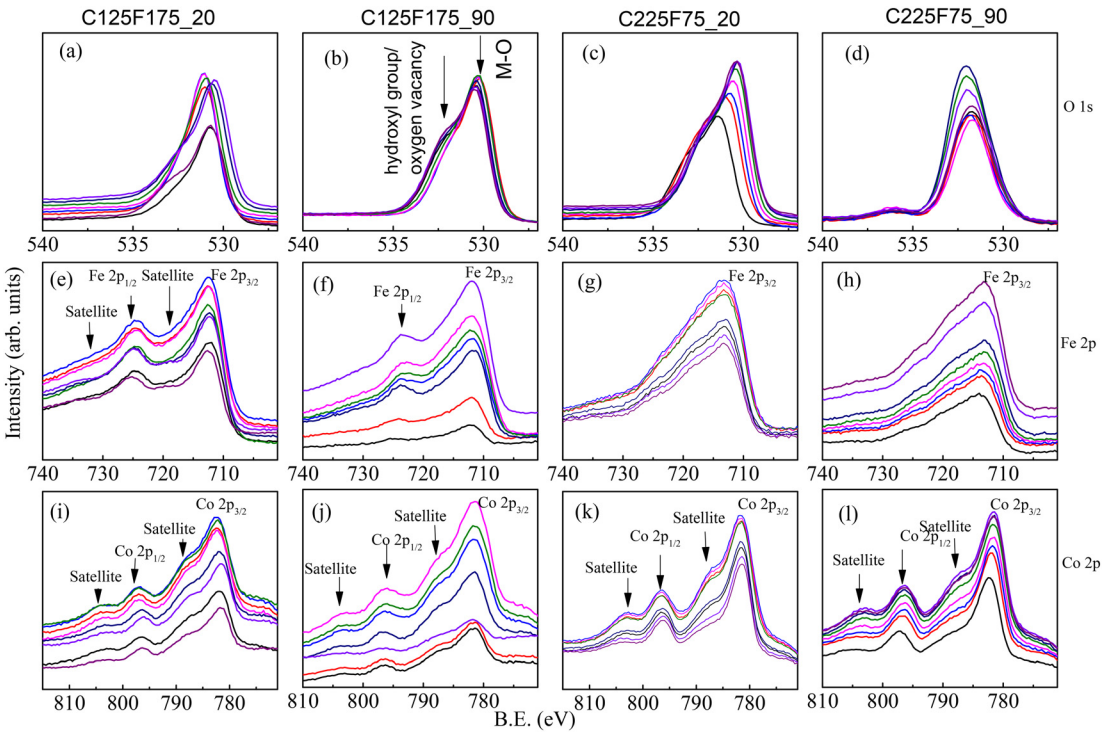

Fig. 5 Line scans of O 1s (a–d), Fe 2p (e–h) and Co 2p (i–l) spectra for C125F175_20, C125F175_90, C225F75_20 and C225F75_90 samples. The peak profile components are marked for O 1s, Fe 2p and Co 2p bands.

equilibrium structure is more prominent for the samples prepared at 200 °C (C125F175_20 and C225F75_20), where the peak component for lattice-oxygen showed a considerable shift when recorded at different points. On the other hand, the samples prepared at 900 °C showed well-defined positions (B. E. ~ 530.5 ± 0.1 eV for C125F175_90 and 531.8 ± 0.1 eV for C225F75_90) for the peak component corresponding to lattice-oxygen and confirms a stable lattice structure. The Fe 2p (Fig. 5(e–h)) and Co 2p (Fig. 5(i–l)) band profiles are reproducible at different points of the line scan and some characteristic changes can be seen in the spectra when Co content in the spinel ferrite increases. The Fe 2p band exhibited a well-defined split ($2p_{3/2}$ and $2p_{1/2}$ sub-bands due to spin–orbit coupling) for the samples of $Co_{1.25}Fe_{1.75}O_4$ composition (first and second columns), whereas the $2p_{3/2}$ sub-band dominates over the $2p_{1/2}$ sub-band for the samples of $Co_{2.25}Fe_{0.75}O_4$ composition (third and fourth columns). The peak intensity (I) in the spectral band is directly proportional to $(2J + 1)\exp(-E_J/k_BT)$, where $2J + 1$ is the multiplicity factor and E_J is the energy level of specific sub-bands. The total quantum

Table 2 XPS peak parameters (binding energy and area) obtained from deconvolution of 2p and 3s bands

		Fe 2p			Co 2p			Fe 3s			Co 3s		
Samples	Peak no.	B.E (eV)	β (eV)	Δ (eV)	B.E (eV)	β (eV)	Δ (eV)	B.E (eV)	β (eV)	Δ (eV)	B.E (eV)	β (eV)	Δ (eV)
Co125F175_20	1	710.34(6)	2.87(2)	Δ = 12.83	780.37(1)	2.13(1)	Δ = 15.80	92.83(3)	3.30(1)	—	100.63(4)	4.22(2)	Δ_{3s} = 4.64
	2	712.24(6)	3.99(5)	Δ_1 = 5.25	782.22(4)	2.91(2)	Δ_1 = 6.00	93.84(3)	3.01(8)	Fe^{2+}/Fe^{3+} = 0.32	102.65(4)	1.22(4)	Co^{3+}/Co^{2+} = 0.75
	3	716.35(3)	7.81(3)	Δ_2 = 6.00	786.84(6)	3.90(1)	Δ_2 = 7.00				106.49(5)	3.80(7)	
	4	724.03(2)	3.66(6)	Fe^{2+}/Fe^{3+} = 0.81	789.72(1)	4.51(5)	Co^{3+}/Co^{2+} = 0.62						
	5	728.12(3)	9.01(2)		797.01(4)	3.99(2)							
	6				803.49(3)	4.86(2)							
Site distribution of cations from SXRD refinement $(Co_{0.63}Fe_{0.37})_A[Co_{0.62}Fe_{1.38}]_B$, from XPS $(Co^{2+}_{0.74}Fe^{3+}_{0.26})_A[Co^{3+}_{0.51}Fe^{2+}_{0.78}Fe^{3+}_{0.71}]_B$ and μ = 3.15 μB													
Co125F175_90	1	709.63(4)	3.68(1)	Δ = 12.61	778.50(8)	0.82(2)	Δ = 15.85	92.93(8)	1.65(3)	—	101.19(2)	1.88(1)	Δ_{3s} = 5.00
	2	711.85(6)	4.23(5)	Δ_1 = 5.00	780.17(1)	2.69(8)	Δ_1 = 5.43	93.13(2)	3.82(4)	Fe^{2+}/Fe^{3+} = 0.16	103.01(1)	2.28(1)	Co^{3+}/Co^{2+} = 2.06
	3	715.51(2)	6.47(3)	Δ_2 = 7.00	782.61(2)	2.83(2)	Δ_2 = 6.410				107.51(2)	3.69(2)	
	4	722.91(1)	4.31(3)	Fe^{2+}/Fe^{3+} = 0.80	786.56(1)	4.34(2)	Co^{3+}/Co^{2+} = 0.50						
	5	729.91(4)	5.15(1)		793.56(4)	1.26(1)							
	6				796.21(2)	2.75(1)							
	7				797.99(4)	2.89(2)							
	8				803.46(6)	3.89(1)							
Site distribution of cations from SXRD refinement $(Co_{0.60}Fe_{0.40})_A[Co_{0.65}Fe_{1.35}]_B$, from XPS $(Co^{2+}_{0.55}Fe^{3+}_{0.45})_A[Co^{3+}_{0.70}Fe^{2+}_{0.78}Fe^{3+}_{0.52}]_B$ and μ = 1.82 μB													
Co225F75_20	1	710.08(1)	3.10(4)	Δ = 10.86	773.98(8)	4.73(2)	Δ = 15.99	93.25(1)	2.69(2)	—	102.05(3)	1.68(1)	Δ_{3s} = 5.45
	2	712.45(7)	4.41(1)	Δ_1 = 5.38	780.52(1)	3.61(3)	Δ_1 = 6.10				102.60(1)	3.03(2)	Co^{3+}/Co^{2+} = 4.49
	3	717.16(1)	7.18(2)	Δ_2 = 7.00	785.95(6)	6.97(1)	Δ_2 = 7.00				107.34(1)	3.14(2)	
	4	723.56(2)	4.14(3)	Fe^{2+}/Fe^{3+} = 0.42	796.51(2)	3.94(4)	Co^{3+}/Co^{2+} = 0.30						
	5	728.73(5)	9.63(6)		803.04(3)	4.04(6)							
Site distribution of cations from SXRD refinement $(Co_{0.45}Fe_{0.55})_A[Co_{1.90}Fe_{0.10}]_B$ for Co-rich phase and $(Co_{0.35}Fe_{0.65})_A[Co_{1.80}Fe_{0.20}]_B$ for Fe-rich phase, average of both phases $(Co_{0.40}Fe_{0.60})_A[Co_{1.85}Fe_{0.15}]_B$ from XPS $(Co^{2+}_{0.66}Fe^{3+}_{0.34})_A[Co^{3+}_{1.59}Fe^{2+}_{0.22}Fe^{3+}_{0.19}]_B$ and μ = 1.85 μB													
Co225F75_90	1	709.62(4)	3.22(2)	Δ = 12.39	773.35(7)	4.02(2)	Δ = 16.10	93.22(7)	3.34(2)	—	102.16(2)	4.38(2)	Δ_{3s} = 4.79
	2	711.34(8)	3.57(1)	Δ_1 = 6.50	780.53(2)	4.08(3)	Δ_1 = 5.86				102.94(1)	1.85(3)	Co^{3+}/Co^{2+} = 4.85
	3	714.14(7)	4.60(8)	Δ_2 = 6.50	786.39(7)	5.87(1)	Δ_2 = 6.48				107.34(3)	3.32(5)	
	4	717.97(4)	7.02(6)	Fe^{2+}/Fe^{3+} = 0.29	792.99(1)	1.89(2)	Co^{3+}/Co^{2+} = 0.18						
	5	723.76(1)	2.96(4)		796.63(3)	3.82(9)							
	6	727.61(1)	6.25(5)		803.11(4)	4.01(1)							
Site distribution of cations from SXRD refinement $(Co_{0.70}Fe_{0.30})_A[Co_{1.55}Fe_{0.45}]_B$, from XPS $(Co^{2+}_{0.64}Fe^{3+}_{0.36})_A[Co^{3+}_{1.61}Fe^{2+}_{0.17}Fe^{3+}_{0.22}]_B$ and μ = 1.94 μB													

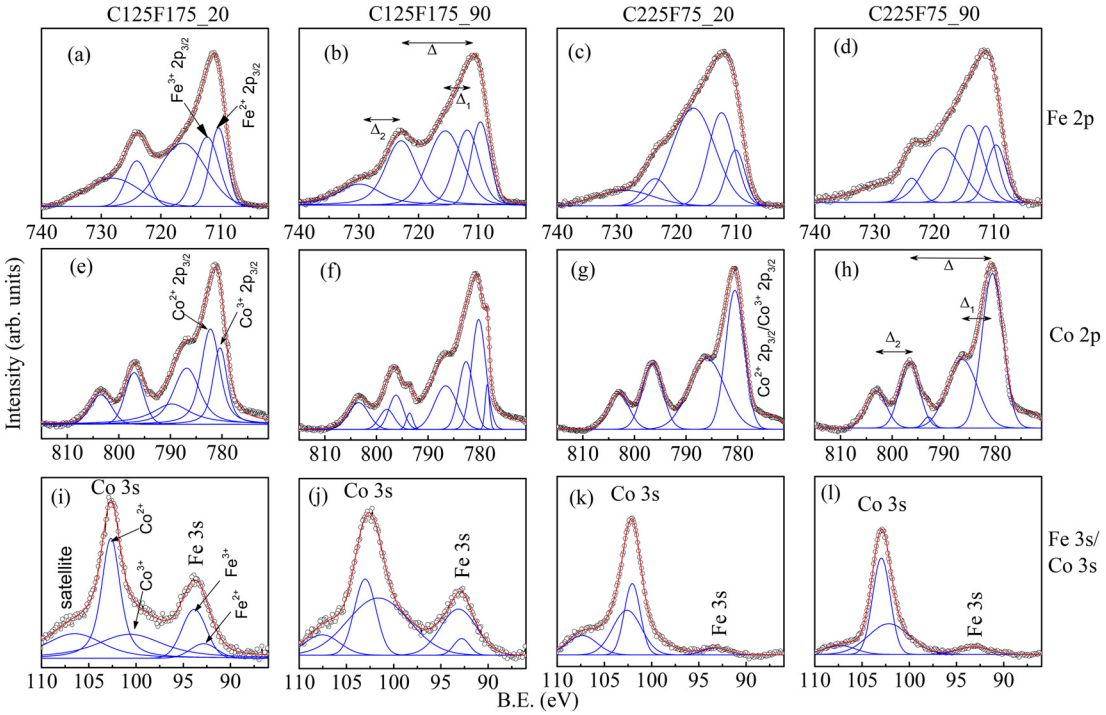

Fig. 6 Deconvulated components of Fe2p (a–d), Co 2p (e–h) and Fe 3s/Co 3s (i–l) spectra for C125F175_20, C125F175_90, C225F75_20 and C225F75_90 samples. The energy difference values and mixed-charge states of Fe and Co ions are marked.

number $J = 3/2$ for the $2p_{3/2}$ sub-band and $J = 1/2$ for the $2p_{1/2}$ sub-band with spin–orbit coupling energy or energy difference, $\Delta = E_{3/2} - E_{1/2}$. It shows that the electrons in the Fe 2p band prefer to occupy the high energetic $2p_{3/2}$ states when the Co content in the Co-rich spinel ferrite increases. The satellite peaks (B.E. ~ 717–719 eV and 732–733 eV) associated with typical +3 charge states of Fe $2p_{3/2}$ and $2p_{1/2}$ sub-bands, respectively[35,36] are suppressed in the samples of $Co_{1.25}Fe_{1.75}O_4$ composition and indicates a mixed-charge (+2/+3) states character of Fe ions.[9,32] The peak profile of the Fe 2p sub-bands widened for the samples of higher Co content ($Co_{2.25}Fe_{0.75}O_4$ composition), and the satellite peaks could be submerged in the broad profiles of the Fe $2p_{3/2}$ and $2p_{1/2}$ sub-bands. The Co 2p band exhibited $2p_{3/2}$ and $2p_{1/2}$ sub-bands and associated satellites for all the samples, but peak profiles of sub-bands and satellites are more distinct and become sharp for the samples with higher Co content ($Co_{2.25}Fe_{0.75}O_4$ composition). The charge states of the Fe and Co ions were understood from the analysis of peak profile parameters (position, full width at half maxima (β) and energy difference components (Δ, Δ_1, Δ_2)) as shown in Table 2 and obtained from deconvolution of the narrow scanned Fe 2p (Fig. 6(a–d)), Co 2p (Fig. 6(e–h)), and Fe 3s/Co 3s (Fig. 6(i–l)) bands by fitting with pseudo-Voigt shape after correction of Shirley type background. The energy difference (Δ: difference between $2p_{3/2}$ and $2p_{1/2}$, Δ_1: difference between $2p_{3/2}$ and its satellite, Δ_2: difference between $2p_{1/2}$ and its satellite, Δ_{3s} = energy difference between Co 3s band and satellite) values were estimated from observed peak positions. The coexistence of mixed-charge states for Fe and Co ions in the present Co-rich spinel ferrite samples can be assigned based on the literature reports.[31–38] The energy difference values (Δ ~ 11–13 eV for Fe 2p and 15.80–16.10 eV for Co 2p) are found within the range of mixed-charge characters. The position and β of the deconvoluted peak components are shown in Table 3. The accuracy of the β values may be affected by the overlapped multiplets and components due to mixed-charge states. In the doublets of the Fe 2p band, the peak components at B.E. ~ 709–710 eV and 723–724 eV correspond to the Fe^{2+} state and the peak components at B.E. ~ 711–714 eV and 725–727 eV correspond to the Fe^{3+} state. In the case of the doublets of the Co 2p band, the peak components at B.E. ~ 780 eV (Co $2p_{3/2}$), 795 eV (Co $2p_{1/2}$) correspond to the Co^{3+} state and the peak components at B.E. ~ 782 eV and 796–797 eV correspond to the Co^{2+} state. The satellite components at B.E. ~ 786 eV correspond to the Co^{2+} state, and 788–789 eV and 803–804 eV correspond to the Co^{3+} state.[32,37] The variation of peak area ratio for the Co 3s and Fe 3s bands confirms the increased Co/Fe ratios, and the Co 3s profile approaches the typical character of Co_3O_4 when the composition changes from $Co_{1.25}Fe_{1.75}O_4$ to $Co_{2.25}Fe_{0.75}O_4$. The peak area ratio of the components in the $2p_{3/2}$ sub-band and 3s band of the Fe and Co ions confirms their mixed-charge characters (coexistence of Fe^{2+}/Fe^{3+} and Co^{3+}/Co^{2+}) in Co-rich spinel ferrites. The quantification of Fe^{2+}/Fe^{3+} and Co^{3+}/Co^{2+} ions from the $2p_{3/2}$ sub-band and 3s band slightly differs due to inaccuracy in the deconvolution of peak components in the presence of multiplicity factors for each charge state, overlapping of the components and co-occupancy at the A- and B-sites of cubic spinel structure.[39] The results in Table 2 suggest that the fraction of the Fe^{2+} state decreases by

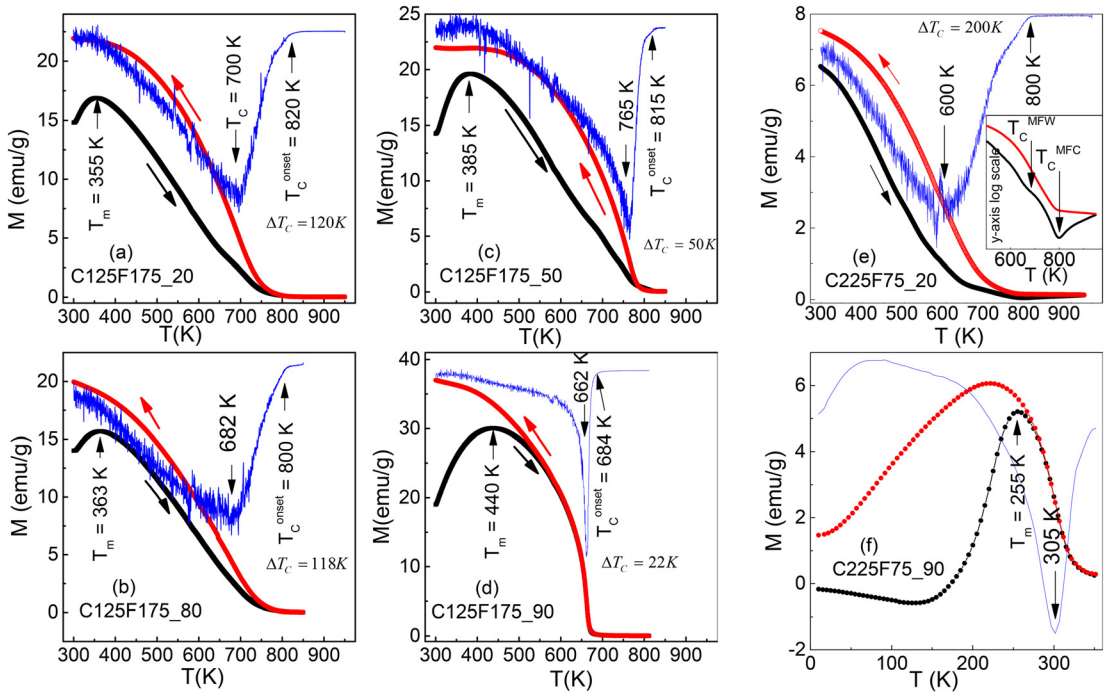

Fig. 7 Temperature dependence of magnetization at 500 Oe in field warming (MFW) and cooling (MFC) modes for different samples of $Co_{1.25}Fe_{1.75}O_4$ composition (a–d) and $Co_{2.25}Fe_{0.75}O_4$ composition (e and f). The temperature derivatives of MFC(T) curves are shown to indicate magnetic transition temperatures (up and down arrows).

increasing the fraction of the Co^{3+} state when the composition changes from $Co_{1.25}Fe_{1.75}O_4$ to $Co_{2.25}Fe_{0.75}O_4$. The site occupancy of the different charge states of Co and Fe ions has been determined from the average site occupancy values from the 2p and 3s bands. The site distribution of Co- and Fe ions from the XPS study is nearly matched to that obtained from Rietveld refinement of SXRD data. It may be suggested that A-sites of the spinel structure will co-occupy Co^{2+} and Fe^{3+} ions, whereas B-sites will co-occupy Co^{2+}/Co^{3+} and Fe^{2+}/Fe^{3+} mixed-charge ions. Generally, the Co^{2+} (~3 μB), Fe^{2+} (~4 μB) and Fe^{3+} (~5 μB) ions at the A- and B-sites prefer high spin states and Co^{3+} (~0 μB) ions at the B-sites prefer low spin state at 0 K.[36] The magnetic moment (μ) per formula unit of the spinel structure from XPS can be realized from dc magnetization measurements.

C. DC magnetization

The temperature-dependent magnetization curves (Fig. 7(a–f)) have been measured during field warming (MFW(T)) and field cooling (MFC(T)) modes under a magnetic field of 500 Oe. The MFC(T) and MFW(T) curves bi-furcated (thermal irreversibility) below the paramagnetic to ferrimagnetic onset temperature (T_C^{onset}) of the samples, where the MFC(T) curve monotonically increased on decreasing the temperature down to 300 K and the MFW(T) curve showed blocking of magnetization below a temperature T_m for all the samples of $Co_{1.25}Fe_{1.75}O_4$ composition (Fig. 7(a–d)). The T_m value increased with the increase in heat treatment temperature in the samples of $Co_{1.25}Fe_{1.75}O_4$. This can be explained by an increase in crystallite size (grain size) and anisotropy energy during the increase in heat treatment temperature.[12,26] It follows a general relation $k_BT_m = 25K_AV_p$, where T_m is the magnetic blocking temperature of the magnetic particle of crystallite size (diameter D) with volume $V_p = (4/3)\pi(D/2)^3$ and anisotropy constant K_A. The MFW(T) curves showed a minor slope change (additional magnetic contribution from minor oxidation of surface ions during higher temperature measurements) in the temperature range of 650–670 K for the samples of $Co_{1.25}Fe_{1.75}O_4$, which were heat treated at lower temperatures (200–800 °C). There is no unusual magnetic upturn in the MFW(T) curve at further higher temperatures, and during field cooling mode from the paramagnetic state, the MFC(T) curve followed the MFW(T) path and bi-furcation (MFC(T) > MFW(T)) started as soon as ferrimagnetic spin order sets in on lowering the measurement temperature. The C125F175_90 sample showed a sharp magnetic transition (T_C ~ 662 K) without any intermediate surface oxidation effect in the MFW(T) curve above T_m and complete reversibility between MFC(T) and MFW(T) curves in the paramagnetic state. In the case of $Co_{2.25}Fe_{0.75}O_4$ composition (Fig. 7(e and f)), T_m is found at ~300 K for the C225F75_20 sample and ~255 K for the C225F75_90 sample. The T_m value in the bi-phased C225F75_20 sample is high (≥300 K) due to the coexistence of a high magnetic Fe-rich phase, and its MFW(T) curve showed an unusual magnetic upturn above the T_C^{onset} ~ 800 K in addition to the observation of an intermediate slope change around 680 K (see inset of Fig. 7(e)). The unusual magnetic upturn in the MFW(T) curve at $T > T_C^{onset}$ arises due

to defect-induced ferrimagnetism in bi-phased Co-rich spinel oxide with two meta-stable magnetic transitions at T_C^{MFW} ~ 675 K and T_0^{MFW} ~ T_C^{MFW} ~ 800 K, respectively.[40] The metastable magnetic spin order is modified during the field cooling process by forming new defect-induced sites in the lattice structure of Co-rich spinel oxides, where the new A sites will be filled by Co^{2+} ions and B sites will be filled by Fe^{3+}/Co^{3+} ions.[3,22] The modification in the metastable spin order arises from the adsorption and ionization of O ions at the defective surface, where a fraction (z) of the Co^{2+} ions at the A sites converts into Co^{3+} ions (through the mechanism $Co^{2+} + \frac{z}{2}O \rightarrow zCo^{3+} + (1-z)\,Co^{2+} + \frac{z}{2}O^{2-}$, whereas a fraction of the Fe^{3+}/Co^{3+} ions at the B sites, highly mobile at high temperatures, diffuses into the surface by creating vacancies at the B sites and forms a skin of γ-Fe_2O_3 like phase in the MFW(T) curve. A rapid exchange between the vacancies and Fe^{3+}/Co^{3+} ions at the B sites and electrons transfer between the interior Co^{2+} ions and surface Fe^{3+}/Co^{3+} ions at the A sites during the field cooling mode leads to a rapid growth of homogenous magnetic spin structure between interior and surface skin. This produces a different MFC(T) path without any local magnetic anomaly in the paramagnetic state and a usual increase of the MFC(T) curve below T_C^{onset} (~ 800 K). The C125F175_90 sample with a stable single-phased lattice structure exhibited stable paramagnetic curves and well-defined T_C. Similarly, the structurally single-phased C225F75_90 sample also showed a well-defined ferrimagnetic to paramagnetic transition at T_C ~ 305 K. The T_C and T_C^{onset} of the samples have been calculated from the temperature derivative of the MFC(T) curves and shown in the right Y–X scales of Fig. 7. The difference (ΔT_C) between T_C and T_C^{onset} decreased with the increase in heat treatment temperature for the $Co_{1.25}Fe_{1.75}O_4$ samples. The bi-phased $Co_{2.25}Fe_{0.75}O_4$ sample showed the highest value of ΔT_C ~ 200 K. The structural meta-stability due to higher temperature surface oxidation effect may be too small to exhibit any additional line in the SXRD pattern for single-phased samples of $Co_{1.25}Fe_{1.75}O_4$ at low-temperature (200–800 °C) heat treatment, but its thermal cyclic induced small hysteresis loop in the cell volume variation, structural parameters and magnetic response, which are sensitive enough to detect the local level non-equilibrium (metastable) states in the measurement temperature scale.

$M(H)$ loops of the samples were recorded in the temperature range of 300–900 K within ±70 kOe but shown within ±20 kOe (Fig. 8(d–f)) for clarity of the loop features. The $M(H)$ curves showed typical ferrimagnetic features with a hysteresis loop and lack of magnetic saturation at higher fields at temperatures below the T_C^{onset}. The ferrimagnetic parameters (coercivity: H_C, remanent magnetization: M_R, saturation magnetization: M_{sat}), as shown in Fig. 8(e–g), were calculated using $M(H)$ loops. The saturated magnetization (M_{sat}) was determined by using the law of approach to saturation of magnetization in the $M(H)$ curves at higher

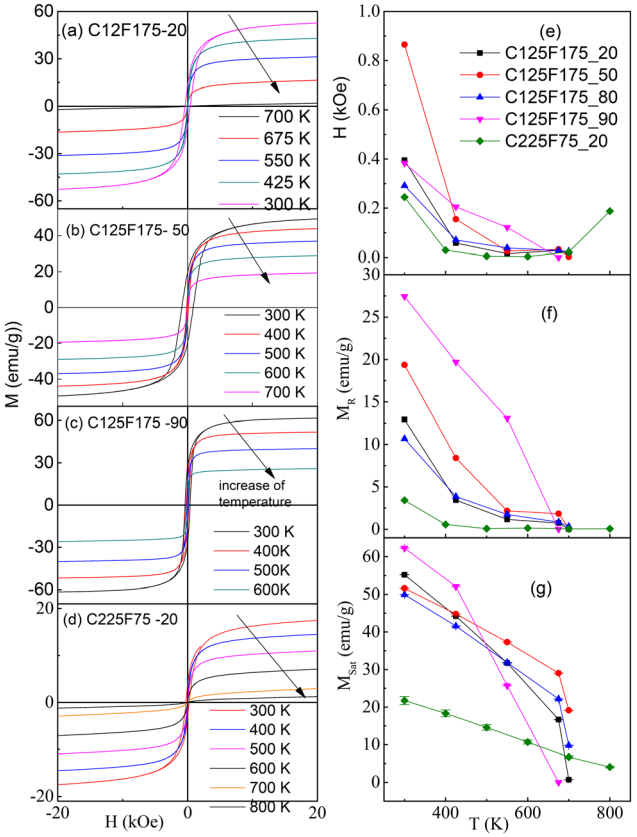

Fig. 8 $M(H)$ loops at selected temperatures (a–d) and the variation in ferrimagnetic parameters (e–g) with temperature for different samples.

fields (>50 kOe). The values of room temperature ferrimagnetic parameters, which were recorded after completing the MFC(T) measurement from 950 K to 300 K, are slightly higher than the values without pre-high temperature MFC(T) measurement of the samples for the $Co_{1.25}Fe_{1.75}O_4$ composition.[26] The bi-phased C225F75_20 sample showed similar differences in the values of magnetic parameters.[41] The saturation magnetic moment values of the samples at room temperature (~55 emu g^{-1} ≈ 2.31 μB for C125F175_20 sample, ~62.5 emu g^{-1} ≈ 2.63 μB for C125F175_90 sample, ~21.8 emu g^{-1} ≈ 0.93 μB for C225F75_20 sample) are found to be slightly smaller than the values calculated from XPS using the maximum (zero-temperature) spin moment values of Co and Fe ions. The values of ferrimagnetic parameters in the samples of $Co_{2.25}Fe_{0.75}O_4$ are smaller due to a higher population of non-magnetic Co^{3+} ions at the B sites than the samples of $Co_{1.25}Fe_{1.75}O_4$ with a higher population of high-magnetic Fe^{2+}/Fe^{3+} ions at the B sites. The ferrimagnetic parameters varied in the single-phased samples of $Co_{1.25}Fe_{1.75}O_4$ depending on the heat treatment temperature and heat treatment at 900 °C exhibited the highest remanent magnetization and high coercivity.[26] The ferrimagnetic parameters usually decreased when the measurement temperature increased from 300 K towards the T_C of the samples. The ferrimagnetic parameters are small in the bi-phased C225F75_20 sample, but its

ferrimagnetic parameters, especially coercivity, have unusually increased at temperatures >700 K due to defect-induced ferrimagnetic phase.[18,22,23] The single-phased (C125F175_90 and C225F75_90) samples exhibited a stable FM–PM transition at T_C, whereas the bi-phased (C225F75_20) sample showed a difference between T_C^{MFW} (~ 675 K) as the T_C for a rigid structure and T_0^{MFW} (~ 800 K) as the T_C for a free structure (which allows defective induced ferrimagnetic state). The defect-induced ferrimagnetic states at $T > T_0^{MFW}$ are frozen during the MFC(T) measurement until the system reaches down to $T_C^{MFC} \sim T_C^{onset}$ for re-establishing the equilibrium ferrimagnetic state.

D. Current–voltage characteristics and electrical conductivity

The effects of equilibrium (single-phased) and non-equilibrium (single-phased and bi-phased) lattice structures on the high-temperature electronic properties were studied by measuring *I–V* curves during the warming (*W*) mode (temperature variation from 300 K to 600 K) and subsequent cooling (*C*) mode from 600 K to 300 K. Fig. 9(a–e) shows the *I–V* characteristics (in *y*-axis log scale) for some of the samples at 350 K and 600 K during the warming mode. The non-linear *I–V* curves confirmed semiconductor features with a highly electric field and thermal-activated enhancement of electrical conductivity. The identical nature of the *I–V* characteristics at the positive and negative bias voltages confirmed good electrical contact on both sides of the samples. The electrical conductivity (σ) at 10 V was calculated from the formula $\sigma = Il/SV$, where l is the length between electrodes and S is the cross-sectional area of the samples. Table 3 compares the conductivity values of the samples at 350 K and 600 K. The heat treatment of the $Co_{1.25}Fe_{1.75}O_4$ composition at 200 °C showed the highest electrical conductivity that gradually decreased by increasing the heat treatment temperature of the samples up to 800 °C and again increased for the heat treatment at 900 °C. This confirms that the kinetic exchange of Co and Fe ions between the intra (B–B)- or inter (A–B)-sites depends on the heat treatment of the samples, especially in the non-equilibrium single-phased structure of Co-rich spinel oxide. The electrical conductivity further decreased in the single-phased C225F75_90 sample with high Co content in comparison to the single-phased C125F175_90 sample. The fact is that hole hopping through Co^{2+}–O^{2-}–Co^{3+} superexchange paths controls p-type semiconductivity for the samples with more Co content (such as $Co_{1.25}Fe_{1.75}O_4$), whereas the electron hopping through Fe^{3+}–O^{2-}–Fe^{2+} superexchange paths controls the n-type semiconductivity for the samples of more Co content (such as $Co_{2.25}Fe_{0.75}O_4$) in $Co_xFe_{3-x}O_4$ spinel structure.[8,42] The temperature dependent-conductivity ($\sigma(T)$) curves in Fig. 9(f–j) showed irreversibility between warming and cooling paths ($\sigma_{cooling}(T) > \sigma_{warming}(T)$) at the higher temperature regime, irrespective of the single- or bi-phased samples. Such irreversible properties in electrical conductivity could be correlated to thermal-induced softness in the bond structure (length, angle and oxygen displacement) and variable range hopping of charge carriers (electrons and holes) *via* the Fe–O–Fe, Co–O–Co and Fe–O–Co superexchange bonds with mixed-charge states at the B-sites of the cubic spinel structure.[43] The retaining of high temperature high-conductive electronic states of the charge carriers (memory of metastable conductivity) during cooling down exhibits a wide loop in ($\sigma(T)$) curves. The metastable conductivity and $\sigma(T)$ loop are found to be maximum for the highly non-equilibrium single-phased C125F175_20 sample, where the current at higher voltage (say 10 V) during the cooling mode exceeded the measurement limit 2 mA using the Keithley meter 6517B (flat $\sigma_{cooling}(T)$ curve at 10 V in the temperature range 653 K to 413 K). The $\sigma(T)$ at 2 V showed the as-usual complete loop like other samples. The defect-induced electronic states are expected at the edges of conduction (CB) and valence (VB) bands for the samples with low heat treatment temperatures (non-equilibrium spinel structure). These additional electronic states act as the centers for trapping/de-trapping electronic charges and contribute to excess electrical conductivity.[44] The electronic spin order and band structure can substantially be modified in the presence of different types of intrinsic point defects ($V_{Co(B)}$, $V_{Fe(A)}$, $V_{Fe(B)}$, V_O, $Co(B)_{Fe(A)}$, $Co(B)_{Fe(B)}$, $Fe(B)_{Co(B)}$, [$Co(B)_{Fe(A)}$, $Fe(A)_{Co(B)}$]) in Co rich spinel oxides.[2,17,21] The $V_{Co(B)}$ is the

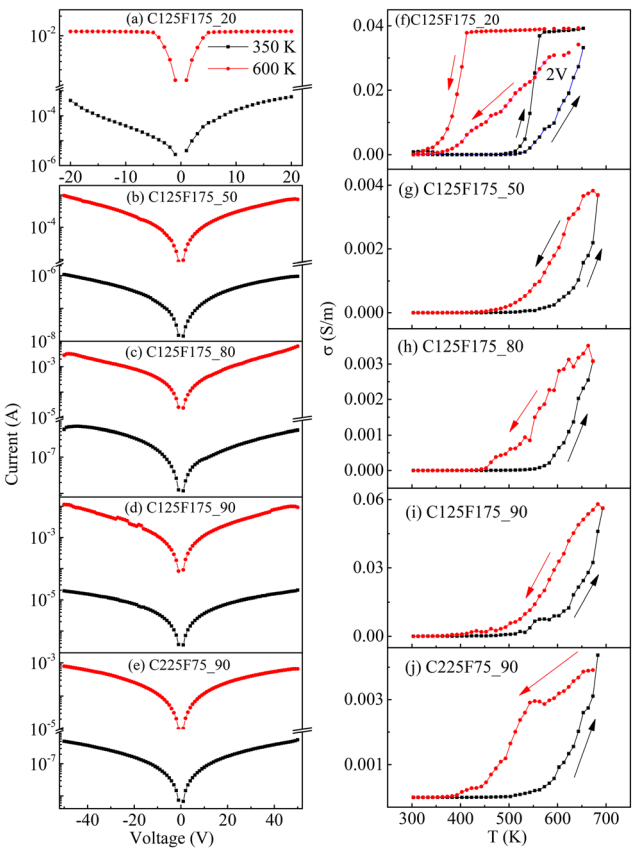

Fig. 9 *I–V* curves at 350 K and 600 K (a–e) and conductivity *vs.* temperature plots at fixed bias voltage (2 V/10 V) during warming and cooling modes of measurement (f–j).

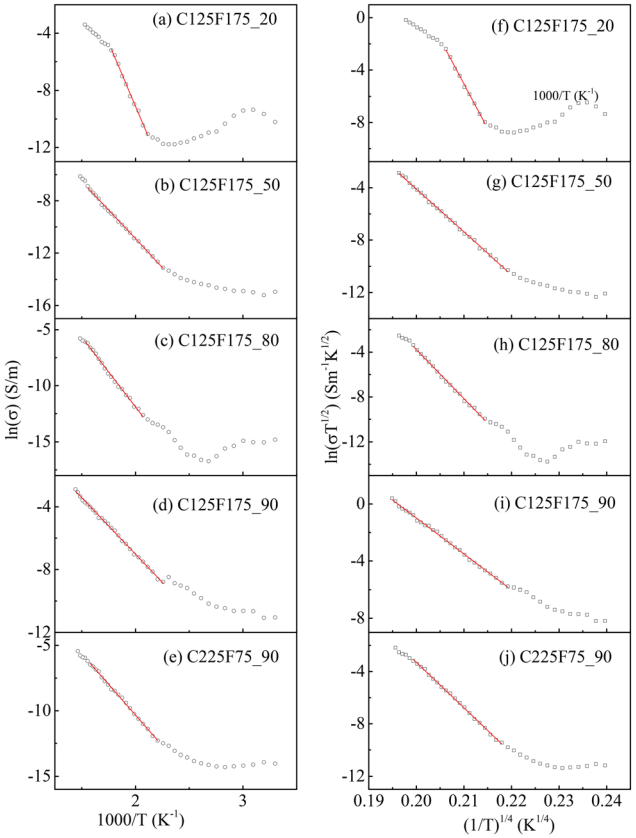

Fig. 10 Fit of $\sigma(T)$ curves during warming mode according to the Arrhenius law (a–e) and Mott variable range hopping mechanism (f–j).

vacancy of Co ions at B sites; $V_{Fe(A)}$ is the vacancy of Fe ions at A sites; $Co(B)_{Fe(A)}$ represents the vacancy of Fe ions at A sites substituted by Co ions at B sites, and $[Co(B)_{Fe(A)}, Fe(A)_{Co(B)}]$ represents the exchange between Co ion at the B site and Fe ion at the A site. The energy required to form $[Co(B)_{Fe(A)}, Fe(A)_{Co(B)}]$ through the kinetic exchange of Fe(A) and Co(B) ions (~0.65 eV) is in the range of activation energy (E_a) of the samples.

The $\sigma_{warming}(T)$ curve at 10 V has been fitted by the equation: $\sigma_{dc}(T) = \sigma_0 T^{-n} \exp\left[-\left(\frac{T_0}{T}\right)^p\right]$ in order to understand the variable hopping mechanism involved, where σ_0 is a constant and T_0 is a characteristic temperature, which corresponds to the required energy for charge hopping, and the exponents n and p depend on the type of charge hopping mechanism.[45,46] In a defect-free semiconductor, the Arrhenius law with $n = 0$ and $p = 0$ describes the thermal-activated long-range hopping of charge carriers (electrons and holes) between two ionic states (separated by the energy gap between the conduction band and valence band). Otherwise, variable range hopping between two electronic states at different ionic sites or band tail states describes the charge conduction mechanism. The Efros–Shklovskii type variable range hopping mechanism ($n = 1$ and $p = \frac{1}{2}$) is applicable for a finite value of Coulomb gap at the Fermi level or Mott type variable-range hopping (MVRH) mechanism ($n = \frac{1}{2}$ and $p = \frac{1}{4}$) is applicable for no gap at the Fermi level.[47] The $\sigma_{warming}(T)$ curves are reasonably well fitted by the Arrhenius mechanism with activation energy ($E_a = k_B T_0$) in the range of 0.6–1.08 eV [insets of Fig. 10(a–e)]. The activation energy is comparable to the values in spinel oxides.[42,48] The C125F175_20 sample, which is expected to have more grain boundary defects, showed an additional activation energy of 1.53 eV at a low-temperature regime. This is due to extended tails in the conduction and valence bands,[49,50] especially at the grain boundaries. According to a theoretical study,[2] high-concentration defects in the Co-rich spinel oxide increase the activation energy, and this can be the case for the C125F175_20 sample. The defect-induced states at higher temperatures are highly sensitive, exhibiting irreversibility in the $\sigma(T)$ curve. The reduction of activation energy in the samples of $Co_{1.25}Fe_{1.75}O_4$ composition by heat treatment at higher temperatures suggests the system slowly approaches the equilibrium state of Co/Fe distribution among the A and B sites of the spinel structure.

Fig. 10(f–j) suggests that the MVRH mechanism[51] is more appropriate to describe $\sigma_{dc}(T)$ curves in the samples according to $\sigma_{dc}(T) = \sigma_0 \cdot T^{\frac{-1}{2}} \exp\left[-\left(\frac{T_0}{T}\right)^{\frac{1}{4}}\right]$ with $\sigma_0 = \frac{3e^2 \vartheta_{ph}}{\sqrt{8\pi}} \left[\frac{N(E_F)}{\alpha K_B T}\right]^{\frac{1}{2}}$ and $T_0 = \left[\frac{24\alpha^3}{K_B N(E_F)}\right]$, where α is the inverse of the length of localized states, $N(E_F)$ is the density of states at the Fermi level, K_B is the Boltzmann constant, and ϑ_{ph} is the phonon frequency

Table 3 The conductivity values of the samples at 350 K and 600 K measured at 10 V/2 V. The fit parameters using Mott variable range hopping at 600 K and activation energy from fitting the Arrhenius equation

	σ (S m^{-1}) at 10 V, 350 K		σ (S m^{-1}) at 10 V, 600 K							
Samples	Warming mode	Cooling mode	Warming mode	Cooling mode	T_0 (K)	α (m^{-1})	$N(E_F)$ (eV^{-1} m^{-3})	R_H (m)	W_H (eV)	E_a (eV)
[a]C125F175_20	5.71×10^{-4}	3.59×10^{-3}	3.84×10^{-3}	3.91×10^{-3}	$2.32(02) \times 10^{11}$	1.91×10^{10}	2.61×10^{24}	1.90×10^{-9}	1.78	0.60/1.53(1)
C125F175_50	4.03×10^{-7}	1.59×10^{-6}	3.92×10^{-4}	2.04×10^{-3}	$1.15(04) \times 10^{10}$	9.47×10^{8}	6.35×10^{21}	1.93×10^{-8}	0.85	0.75(2)
C125F175_80	1.68×10^{-7}	6.05×10^{-7}	6.44×10^{-4}	2.81×10^{-3}	$3.71(03) \times 10^{10}$	3.22×10^{9}	6.41×10^{22}	7.96×10^{-9}	1.14	1.08(3)
C125F175_90	2.87×10^{-5}	1.35×10^{-4}	9.05×10^{-3}	3.28×10^{-2}	$4.07(02) \times 10^{9}$	3.31×10^{8}	7.70×10^{19}	7.43×10^{-8}	0.66	0.62(1)
C225F75_90	6.13×10^{-7}	8.06×10^{-6}	9.27×10^{-4}	3.19×10^{-3}	$1.47(01) \times 10^{10}$	1.26×10^{9}	1.04×10^{22}	1.58×10^{-8}	0.91	0.82(2)

[a] The conductivity of the sample C125F175_20 was measured at 2 V.

($\sim 10^{13}$ s^{-1}) at Debye temperature (typically 900 K for spinel oxide[52]). These parameters were obtained from the slope and intercepts of the $\ln(\sigma_{dc}T^{1/2})$ *vs.* T plots at the higher side of the measurement temperatures. The hopping distance (R_H) and W_H (energy barrier between two ionic sites) have been calculated by the expression $R_H = \left[\frac{1}{8\pi\alpha K_B T N(E_F)}\right]^{\frac{1}{4}}$ and $W_H = 0.25 k_B T_0^{\frac{1}{4}} T^{\frac{3}{4}}$, with T = 600 K. The parameters associated with the MVRH mechanism are shown in Table 3 and are well comparable to the reported values in spinel oxides at measurement temperatures below 300 K.[52] All the samples satisfied $\alpha R_H > 1$, a typical condition for the application of the MVRH mechanism. The MVRH mechanism is generally applicable in the low-temperature regime of electronic materials, where charge carriers can perform a series of variable range hopping between two localized states. Among them, the short-range hopping between nearest neighbours determines the overall charge conductivity. The samples have shown typical hopping lengths (R_H) in the range of 1.9–74.3 nm and energy barriers (W_H) in the range of 0.66–1.78 eV. The fit of the MVRH equation in the present samples suggests that a considerable amount of defect-induced states (donor states near the conduction band and acceptor states near the valence band) overlap about the Fermi level during high-temperature measurements. The signature of a positive slope in the Arrhenius or MVRH plots (Fig. 10) at the temperature range of 300–400 K of the $\sigma(T)$ curves indicates a metal-type conductivity. Such intermediate metal-like conductivity has been observed in many oxides due to the changes in activation energy between the low and high-temperature semiconductor regimes.[21,53,54] The low-temperature semiconductor state below 300 K has not been studied.

4. Conclusions

The synchrotron X-ray diffraction (SXRD) patterns have shown single-phased and bi-phased (Co-rich and Fe-rich) cubic spinel structures in Co-rich spinel ferrites depending on the Co/Fe atomic ratio and heat treatment temperature during material preparation. The existence of intrinsic non-equilibrium (meta-stable) states in the lattice structure, magnetic spin order and electronic conductivity of the samples, irrespective of the single- or bi-phased structure, has been confirmed from high-temperature measurements during warming and cooling modes. The cell volume followed a reversible path during the warming and cooling modes of the measurements for stable single-phased samples. The cell volume in the samples of non-equilibrium lattice structure (single-phase for $Co_{1.25}Fe_{1.75}O_4$ composition and bi-phase for $Co_{2.25}Fe_{0.75}O_4$ composition) showed irreversible paths in the measurement temperature range of 473–773 K, whereas the cell volume followed reversible paths in the samples of equilibrium (stable) lattice structures from SXRD measurements. The oxygen parameter and site occupancy of Co/Fe ions followed irreversible paths irrespective of the single- or bi-phased samples. The samples of non-equilibrium lattice structures exhibited additional metastable magnetic contribution in the form of local magnetic distortion due to surface oxidation or defect-induced ferrimagnetic phase. The (stable) single-phased samples showed a well-defined paramagnetic to ferrimagnetic transition (T_C) without an intermediate metastable magnetic state. On the other hand, electrical conductivity curves, irrespective of the single- and bi-phased cubic spinel structure, exhibited thermal hysteresis and variable non-equilibrium charge dynamics due to mixed-charge states of Co and Fe ions at the B-sites. This work shows that a unified picture of the equilibrium or non-equilibrium state cannot be verified simultaneously for all physical properties parameters, even in the material of single-phase structures from SXRD patterns. The suitable tuning of the non-equilibrium lattice structure, ferrimagnetic spin order and electrical conductivity can be useful for high-temperature applications of spinel oxides in the field of high energy magneto-electric memory devices.

Data availability

The data have been recorded in collaboration with different research groups and are confidential in nature. However, specific requests can be considered for providing the data and necessary information.

Conflicts of interest

There are no conflicts to declare.

Acknowledgements

RNB acknowledges the Research Grant from UGC-DAE CRS project (No. CRS/2021-22/03/560) for completing this collaborative work and RRCAT-Indus 2, Indore, for providing high-temperature synchrotron X-ray diffraction measurement facilities. RNB thanks Dr. Archana Sagdeo and Mr. M. N. Singh for assisting in SXRD measurements.

References

1 A. Walsh, Su-H. Wei, Y. Yan, M. M. Al-Jassim and J. A. Turner, Structural, magnetic, and electronic properties of the Co-Fe-Al oxide spinel system: Density-functional theory calculations, *Phys. Rev. B: Condens. Matter Mater. Phys.*, 2007, **76**, 165119.
2 Y. L. Huang, W. B. Fan, Y. H. Hou, K. X. Guo, Y. F. Ouyang and Z. W. Liu, Effects of intrinsic defects on the electronic structure and magnetic properties of CoFe2O4: A first-principles study, *J. Magn. Magn. Mater.*, 2017, **429**, 263.
3 I. Kupchak and N. Serpak, Electronic and Magnetic Properties of Spinel Co3O4 (111) Surface in GGA+U Approximation, *Ukr. J. Phys.*, 2017, **62**, 615.

4 T. M. C. Dinh, A. Barnabé, M. A. Bui, C. Josse, T. Hungria, C. Bonningue and L. Presmanes, Tailhades, P. FIB plan view lift-out sample preparation for TEM characterization of periodic nanostructures obtained by spinodal decomposition in $Co_{1.7}Fe_{1.3}O_4$ thin films, *CrystEngComm*, 2018, **20**, 6146.

5 K. Hayashi, K. Yamada and M. Shima, Compositional dependence of magnetic anisotropy in chemically synthesized $Co_{3-x}Fe_xO_4$ ($0 \leq x \leq 2$), *Jpn. J. Appl. Phys.*, 2018, **57**, 01AF02.

6 S. R. Liu, D. H. Ji, J. Xu, Z. Z. Li, G. D. Tang, R. R. Bian, W. H. Qi, Z. F. Shang and X. Y. Zhan, Estimation of cation distribution in spinel ferrites $Co_{1+x}Fe_{2-x}O_4$ ($0.0 \leq x \leq 2.0$) using the magnetic moments measured at 10 K, *J. Alloys Compd.*, 2013, **581**, 616–624.

7 H. L. Trong, L. Presmanes, E. D. Grave, A. Barnabe and C. Bonningue, pH Tailhades. Mössbauer characterisations and magnetic properties of iron cobaltites CoxFe3−xO4 ($1 \leq x \leq 2.46$) before and after spinodal decomposition, *J. Magn. Magn. Mater.*, 2013, **334**, 66.

8 N. Bahlawane, P. H. T. Ngamou, V. Vannier, T. Kottke, J. Heberle and K. K. Hoinghaus, Tailoring the properties and the reactivity of the spinel cobalt oxide, *Phys. Chem. Chem. Phys.*, 2009, **11**, 9224.

9 W. Xiang, *et al.*, 3D atomic-scale imaging of mixed Co-Fe spinel oxide nanoparticles during oxygen evolution reaction, *Nat. Commun.*, 2022, **13**, 179.

10 I. P. Muthuselvam and R. N. Bhowmik, Structural phase stability and magnetism in Co2FeO4 spinel oxide, *Solid State Sci.*, 2009, **11**, 719.

11 M. R. Panda, R. N. Bhowmik, H. Singh, M. N. Singh and A. K. Sinha, Air annealing effects on lattice structure, charge state distribution of cations, and room temperature ferrimagnetism in the ferrite composition Co2.25Fe0.75O4, *Mater. Res. Express*, 2015, **2**, 036101.

12 R. N. Bhowmik, S. Kazhugasalamoorthy, R. Ranganathan and A. K. Sinha, Tuning of composite cubic spinel structure in Co1.75Fe1.25 O4 spinel oxide by thermal treatment and its effects on modifying the ferromagnetic properties, *J. Alloys Compd.*, 2016, **680**, 315.

13 A. Mikhail, *et al.*, High-Temperature Ferromagnetism of the Iron-Based FCC Phase: The Effect of Carbon and Nickel, *Phys. Status Solidi B*, 2022, **259**, 2200248.

14 K. L. Routray, D. Sanyal and D. Behera, Dielectric, magnetic, ferroelectric, and Mossbauer properties of bismuth substituted nanosized cobalt ferrites through glycine nitrate synthesis method, *J. Appl. Phys.*, 2017, **122**, 224104.

15 N. Debnath, *et al.*, Magnetic-field-induced phase separation via spinodal decomposition in epitaxial manganese ferrite thin films, *Sci. Technol. Adv. Mater.*, 2018, **19**, 507–516.

16 H. C. O'Neill, S. A. T. Redfern, S. Kesson and S. Short, An in situ neutron diffraction study of cation disordering in synthetic qandilite Mg2TiO4 at high temperatures, *Am. Mineral.*, 2003, **88**, 860.

17 S. M. Antao, I. Hassan and J. B. Parise, Cation ordering in magnesioferrite, MgFe2O4, to 982 °C using in situ synchrotron X-ray powder diffraction, *Am. Mineral.*, 2005, **90**, 219.

18 C. E. R. Torres, Oxygen-vacancy-induced local ferromagnetism as a driving mechanism in enhancing the magnetic response of ferrites, *Phys. Rev. B: Condens. Matter Mater. Phys.*, 2014, **89**, 104411.

19 P. W. Readman and W. O'Reilly, Magnetic Properties of Oxidized (Cation-Deficient) Titanomagnetites (Fe, Ti)$_3O_4$, *J. Geomagn. Geoelectr.*, 1972, **24**, 69.

20 Y. Zhang, Z. Yang, B.-P. Zhu, J. Ou-Yang, R. Xiong, X.-F. Yang and S. Chen, Exchange bias effect of $Co_{3-x}Fe_xO_4$ (x = 0, 0.09, 0.14 and 0.27), *J. Alloys Compd.*, 2012, **514**, 25.

21 M. C. Aswathi and R. N. Bhowmik, Meta-stable magnetic transitions and its field dependence in Co2.75Fe0.25O4 ferrite, *AIP Conf. Proc.*, 2018, **1942**, 130023.

22 R. N. Bhowmik, P. D. Babu, A. K. Sinha and A. Bhiskar, High-Temperature Thermal Cycling Effect on the Irreversible Responses of Lattice Structure, Magnetic Properties, and Electrical Conductivity in Co2.75Fe0.25O4+δ Spinel Oxide, *Inorg. Chem.*, 2020, **59**, 6763.

23 S. Bustingorry, F. Pomiro, G. Aurelio and J. Curiale, Second-order magnetic critical points at finite magnetic fields: Revisiting Arrott plots, *Phys. Rev. B*, 2016, **93**, 224429.

24 K. K. Nielsen, C. R. H. Bahl, A. Smith and R. Bjørk, Spatially resolved modelling of inhomogeneous materials with a first order magnetic phase transition, *J. Phys. D: Appl. Phys.*, 2017, **50**, 414002.

25 Q. Sun, M. Zhu, Q. Wang, C. Zhu, J. Yang and W. Li, Design of novel quasi-trivalent dual-main-phase Ce magnets with high performance by manipulating the chemical state of Ce, *Acta Mater.*, 2023, **246**, 118703.

26 R. N. Bhowmik and A. K. Sinha, Improvement of room temperature electric polarization and ferrimagnetic properties of Co1.25Fe1.75O4 ferrite by heat treatment, *J. Magn. Magn. Mater.*, 2017, **421**, 120.

27 R. N. Bhowmik, A. Kumar and S. M. Yusuf, Understanding of the low temperature anomalous magnetic and lattice properties in Co1.25Fe1.75O4 ferrite using dc magnetization and neutron diffraction experiments, *J. Magn. Magn. Mater.*, 2019, **485**, 331.

28 H. St. C. O'Neill and A. Navrotsky, Simple spinels; crystallographic parameters, cation radii, lattice energies, and cation distribution, *Am. Mineral.*, 1983, **68**, 181.

29 J. M. Hastings and L. M. Corliss, Neutron Diffraction Studies of Zinc Ferrite and Nickel Ferrite, *Rev. Mod. Phys.*, 1953, **25**, 114.

30 R. Verma, S. N. Kane, P. Tiwari, S. S. Modak, T. Tatarchuk and F. Mazaleyrat, *Mol. Cryst. Liq. Cryst.*, 2018, **674**, 130–141.

31 R. Li, B. Hu, T. Yu, H. Chen, Y. Wang and S. Song, Insights into Correlation among Surface-Structure-Activity of Cobalt-Derived Pre-Catalyst for Oxygen Evolution Reaction, *Adv. Sci.*, 2020, **7**, 1902830.

32 S. Magalhães, P. Bargiel, M. Graça, C. Rocha, E. S. Gild and A. R. Souza, Iron Cobaltite (FeCo2O4) Nanocatalysts for Water-Oxidation: Effects of Annealing Temperature on Catalytic Properties, *J. Braz. Chem. Soc.*, 2022, **33**, 1163–1171.
33 K. M. Cole, D. W. Kirk and S. J. Thorpe, Co3O4 nanoparticles characterized by XPS and UPS, *Surf. Sci. Spectra*, 2021, **28**, 014001.
34 Y. Xu, H. Zhang, D. Gong, Y. Chen, S. Xu and P. Qiu, Solar water splitting with nanostructured hematite: the role of oxygen vacancy, *J. Mater. Sci.*, 2022, **57**, 19716–19729.
35 V. Sahoo, R. N. Bhowmik and S. A. Khan, Enhancement of electrical conductivity, optical band gap and ferromagnetic properties by co-doping of Co and Ti ions in canted antiferromagnetic hematite (α-Fe2O3) system, *Mater. Chem. Phys.*, 2023, **296**, 127298.
36 Yu. A. Teterin, *et al.*, Electronic Structure of Cobaltites ScCo1 – xFexO3 (x = 0, 0.05) and BiCoO3: X-Ray Photoelectron Spectroscopy, *J. Exp. Theor. Phys.*, 2019, **128**, 899–908.
37 Y. Lou, *et al.*, Promoting Effects of In2O3 on Co3O4 for CO Oxidation: Tuning O2 Activation and CO Adsorption Strength Simultaneously, *ACS Catal.*, 2014, **4**, 4143–4152.
38 R. E. El-Shater, *et al.*, Fabrication of doped ferrites and exploration of their structure and magnetic behavior, *Mater. Adv.*, 2023, **4**, 2794.
39 M. Oku and K. Hirokawa, X-ray photoelectron spectroscopy of Co304, Fe304, MnO, and related compounds, *J. Electron Spectrosc. Relat. Phenom.*, 1976, **8**, 475–481.
40 R. Nepal, Q. Zhang, S. Dai, W. Tian, S. E. Nagler and R. Jin, Structural and magnetic transitions in spinel FeMn2O4 single crystals, *Phys. Rev. B*, 2018, **97**, 024410.
41 R. N. Bhowmik, G. Kishor, D. Sherin, A. Kumar, P. D. Babu and S. M. Yusuf, Effects of intrinsic and extrinsic multi-phased lattice structure and chemical heterogeneity on the control of ferrimagnetic properties in Co rich spinel ferrite, *J. Magn. Magn. Mater.*, 2023, **588**, 171412.
42 G. H. Jonker, Analysis of the semiconducting properties of cobalt ferrite, *J. Phys. Chem. Solids*, 1959, **9**, 165.
43 Y. Shi, *et al.*, Self-Doping and Electrical Conductivity in Spinel Oxides: Experimental Validation of Doping Rules, *Chem. Mater.*, 2014, **26**, 1867.
44 M. Younas, M. Nadeem, M. Atif and R. Grossinger, Metal-semiconductor transition in NiFe2O4 nanoparticles due to reverse cationic distribution by impedance spectroscopy, *J. Appl. Phys.*, 2011, **109**, 093704.
45 M. Z. Ansari and N. Kharea, Thermally activated band conduction and variable range hopping conduction in Cu2ZnSnS4 thin films, *J. Appl. Phys.*, 2015, **117**, 025706.
46 R. N. Bhowmik and R. Ranganathan, Magnetic order and electrical conductivity scaling of the spinel oxide Mn0.5Ru0.5Co2O4, *Phys. Rev. B: Condens. Matter Mater. Phys.*, 2006, **74**, 214417.
47 N. Aghashahi, M. R. Mohamadizadeh and P. Kameli, Variable range hopping conduction mechanisms in reduced rutile TiO2, *Phys. Scr.*, 2022, **97**, 045408.
48 R. N. Bhowmik and K. S. Aneesh Kumar, Role of pH value during material synthesis and grain-grain boundary contribution on the observed semiconductor to metal like conductivity transition in Ni1.5Fe1.5O4 spinel ferrite, *Mater. Chem. Phys.*, 2016, **177**, 417.
49 H. Taz, *et al.*, Integration of amorphous ferromagnetic oxides with multiferroic materials for room temperature magnetoelectric spintronics, *Sci. Rep.*, 2020, **10**, 3583.
50 R. Plugaru, T. Sandu and N. Plugaru, First principles study and variable range hopping conductivity in disordered Al/Ti/Mn-doped ZnO, *Results Phys.*, 2012, **2**, 190.
51 L. Chauhan, S. Kumar, K. Sreenivas and A. K. Shukla, Variable range hopping and modulus relaxation in NiFe2O4 ceramics, *Mater. Chem. Phys.*, 2021, **259**, 124135.
52 C. M. Fang, C. K. Loong, G. A. de Wejis and G. de With, Phonon spectrum of $ZnAl_2O_4$ spinel from inelastic neutron scattering and first-principles calculations, *Phys. Rev. B: Condens. Matter Mater. Phys.*, 2002, **66**, 144301.
53 R. N. Bhowmik and A. G. Lone, Dielectric properties of α-$Fe_{1.6}Ga_{0.4}O_3$ oxide: A promising magneto-electric material, *J. Alloys Compd.*, 2016, **680**, 31.
54 R. N. Bhowmik and K. S. Aneesh Kumar, Role of pH value during material synthesis and grain-grain boundary contribution on the observed semiconductor to metal like conductivity transition in $Ni_{1.5}Fe_{1.5}O_4$ spinel ferrite, *Mater. Chem. Phys.*, 2016, **177**, 417.